

# Iterative methods for the reconstruction of astronomical images with high dynamic range

B. Anconelli<sup>a</sup>, M. Bertero<sup>a,\*</sup>, P. Boccacci<sup>a</sup>, M. Carillet<sup>b</sup>, H. Lanteri<sup>b</sup>

<sup>a</sup>*DISI, Università di Genova, Via Dodecaneso 35, I-16146 Genova, Italy*

<sup>b</sup>*Laboratoire Universitaire d'Astrophysique de Nice, UMR 6525, Parc Valrose, 06108 Nice, Cedex 02, France*

Received 12 November 2004; received in revised form 21 June 2005

## Abstract

In most cases astronomical images contain objects with very different intensities such as bright stars combined with faint nebulae. Since the noise is mainly due to photon counting (Poisson noise), the signal-to-noise ratio may be very different in different regions of the image. Moreover, the bright and faint objects have, in general, different angular scales. These features imply that the iterative methods which are most frequently used for the reconstruction of astronomical images, namely the Richardson–Lucy Method (RLM), also known in tomography as Expectation Maximization (EM) method, and the Iterative Space Reconstruction Algorithm (ISRA) do not work well in these cases. Also standard regularization approaches do not provide satisfactory results since a kind of *adaptive* regularization is required, in the sense that one needs a different regularization for bright and faint objects. In this paper we analyze a number of regularization functionals with this particular kind of adaptivity and we propose a simple modification of RLM and ISRA which takes into account these regularization terms. The preliminary results on a test object are promising.

© 2005 Elsevier B.V. All rights reserved.

*Keywords:* Image reconstruction; Regularization; Iterative methods

## 1. Introduction

Astronomical images are degraded by blurring and noise (photon noise, read-out-noise, etc.). In many circumstances the blurring can be described by a space-invariant Point Spread Function (PSF) which takes into account the effects of diffraction and, in the case of ground-based telescope, of atmospheric turbulence (including Adaptive Optics corrections). Therefore, a modeling of the image formation process and the use of deconvolution methods are required to improve the quality of the detected images.

Several iterative methods have been proposed for image deconvolution with the constraint of non-negativity. However only a few of them are frequently used in practice: we mention RLM and ISRA which will be considered in the next sections. These methods may not work well in the case of images with high dynamic range, namely images where objects with very different brightness are present in the same field. An example, which will be used as a test object for our numerical simulations, is shown in Fig. 1 (upper-left panel). It is a model of young binary star consisting of a core

\* Corresponding author. Tel: +39 010 3536733; fax: +39 010 3536699.

E-mail address: [bertero@disi.unige.it](mailto:bertero@disi.unige.it) (M. Bertero).

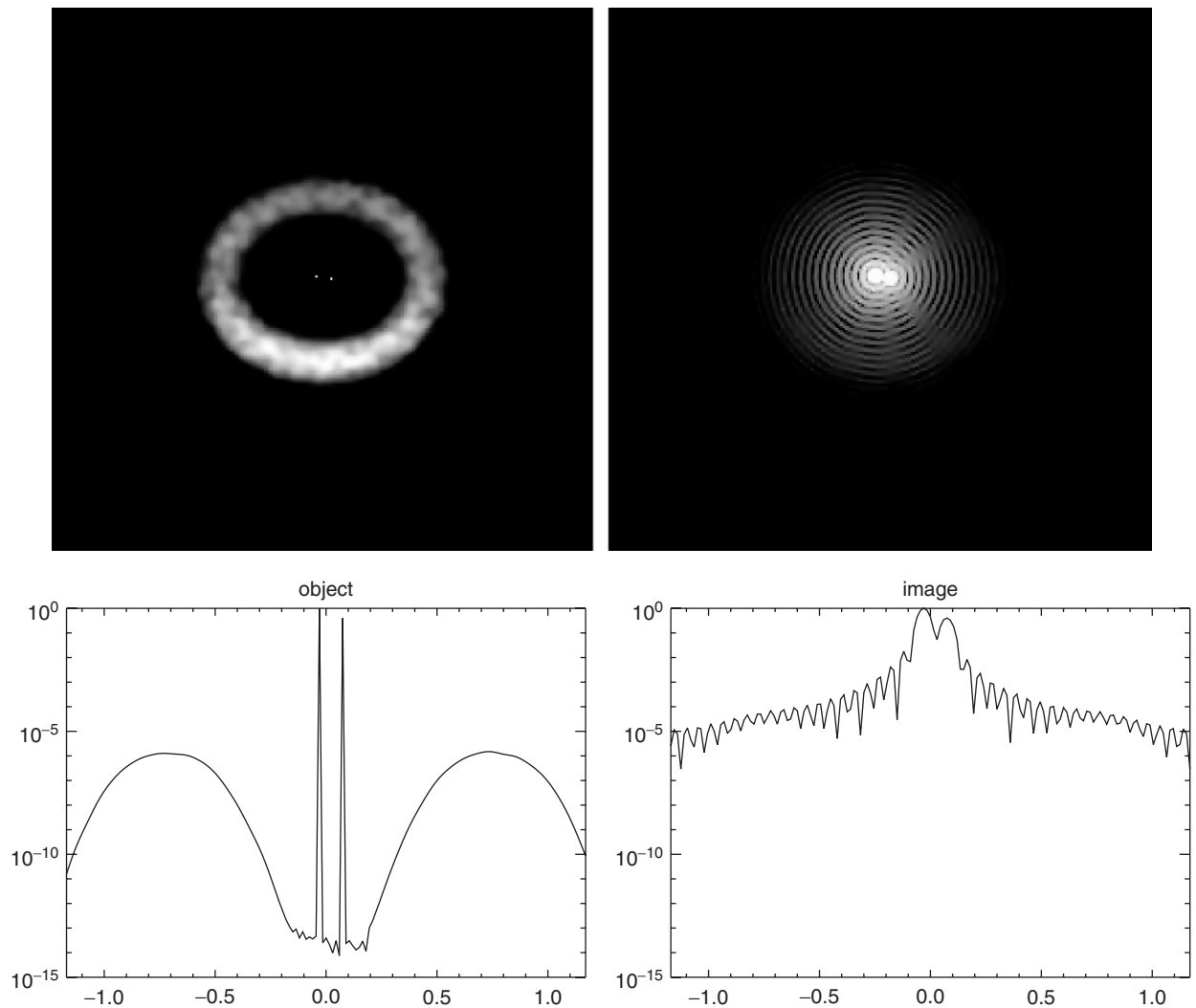


Fig. 1. Upper panels: gray level representation of the model of young binary star [left] and of its image provided by a perfect circular mirror [right]. Lower panels: cuts of the object [left] and of its image [right] along the direction of the binary system.

binary surrounded by a dusty circumbinary ring [2], directly inspired by the T-Tauri binary star of the quadruple system *GG Tau*. In the same figure (upper-right panel) we show the image which is obtained by convolving the object with the PSF of a perfect circular mirror; the angular resolution of the mirror is just allowing the separation of the two stars. This picture makes clear the need of deconvolving the detected image because the circumbinary ring is completely corrupted by the side lobes of the image of the binary star, due to the side lobes of the PSF of the mirror (the so-called Airy function). This effect is further explained in the lower panels of Fig. 1. In the lower-left panel we give the cut of the object along the direction of the binary star: the ratio between the brightness of the stars and the brightness of the ring is of the order of  $10^6$ , and therefore is much greater than the ratio between the central lobe and the side lobes of the PSF. Moreover, the cut of the image along the same direction, given in the lower-right panel, shows that the structure of the ring is hidden by the side lobes of the PSF.

In this paper we propose and discuss a few regularized algorithms for the reconstruction of objects satisfying the following conditions:

- there is a gap between the magnitudes of the point and of the diffuse objects (for instance, the point objects are much brighter than the others);

- there is an angular separation between the two kinds of objects, i.e. they are located in different regions of the image domain.

The regularization methods we propose are *adaptive* in the sense that they provide a different kind of regularization for point and diffuse objects. They contain two parameters: a *thresholding parameter*, separating the intensities of bright and faint objects and a *regularization parameter*, which is essentially a Tikhonov regularization parameter, for a smooth reconstruction of the diffuse objects. The evaluation of the thresholding parameter can be obtained from a preliminary reconstruction of the object, as provided by one of the standard methods (for instance RLM). In this preliminary study no automatic choice of the parameters is investigated.

The iterative algorithms for the minimization of the regularized functionals are obtained by means of a simple modification of RLM and/or ISRA, with no substantial increase of the computational cost per iteration. In Section 2 we briefly describe a general approach to the design of these iterative methods for image reconstruction and we derive the general form of the regularized versions of RLM and ISRA. In Section 3 we introduce the regularization functionals we investigate for the reconstruction of high-dynamic images and finally in Section 4 we discuss the numerical results we have obtained in the case of the test object of Fig. 1.

## 2. The split gradient method

We denote by  $\mathbf{g}$  the array of the detected image, which is the realization of a random process  $\mathbf{G}$  with expected value:

$$E\{\mathbf{G}\} = \mathbf{A}\mathbf{f} + \mathbf{b}, \tag{1}$$

where  $\mathbf{f}$  is the array of the unknown object,  $\mathbf{A}$  is the matrix describing the blurring and  $\mathbf{b}$  is a background term (approximately constant over the image domain) which is due to the diffuse emission of the sky and of the detector. If the imaging system is approximately space invariant and if it is possible to neglect boundary effects (as in the case of the object of Fig. 1), then the matrix  $\mathbf{A}$  can be approximated by the cyclic convolution with the PSF  $\mathbf{K}$  of the system:

$$\mathbf{A}\mathbf{f} = \mathbf{K} * \mathbf{f}. \tag{2}$$

In image reconstruction, the aim is to obtain an estimate of the unknown object  $\mathbf{f}$ , being given the detected image  $\mathbf{g}$ , the PSF  $\mathbf{K}$ , and the background  $\mathbf{b}$ . In regularization theory or in maximum likelihood and Bayesian approaches, the problem is formulated in terms of the minimization of a suitable functional.

We denote by  $J(\mathbf{f}; \mathbf{g})$  this functional. Then, in the case of astronomical images one must consider additional constraints and, in particular non-negativity and flux conservation, i.e. the minima must be searched in the domain of the objects  $\mathbf{f}$  satisfying the conditions

$$\mathbf{f}(m, n) \geq 0, \quad \sum_{m,n} \mathbf{f}(m, n) = \sum_{m,n} \mathbf{g}(m, n) \doteq c, \tag{3}$$

where  $m, n$  is a pair of indexes running over the pixels of the image.

An approach to the design of iterative methods for constrained minimization was proposed by Lanteri and coworkers [11,10]. This approach is called split gradient method (SGM) because it is based on the following decomposition of the gradient of the functional:

$$-\nabla_{\mathbf{f}} J(\mathbf{f}; \mathbf{g}) = \mathbf{U}(\mathbf{f}; \mathbf{g}) - \mathbf{V}(\mathbf{f}; \mathbf{g}), \tag{4}$$

where  $\mathbf{U}(\mathbf{f}; \mathbf{g})$  and  $\mathbf{V}(\mathbf{f}; \mathbf{g})$  are positive arrays depending on  $\mathbf{f}$ . Obviously such a decomposition always exists and is not unique. The applicability of the method requires explicit expressions for the dependence of these arrays on  $\mathbf{f}$ .

The constrained minimization of the functional  $J(\mathbf{f}; \mathbf{g})$  can be reduced to the minimization of the Lagrange function given by

$$L(\mathbf{f}, \lambda, \gamma; \mathbf{g}) = J(\mathbf{f}; \mathbf{g}) - (\lambda, \mathbf{f}) + \gamma \left( \sum_{m,n} \mathbf{f}(m, n) - \sum_{m,n} \mathbf{g}(m, n) \right), \tag{5}$$

where  $\lambda$  is the array of the Lagrange multipliers ( $\lambda(m, n) \geq 0$ , for any  $m, n$ ) associated with the non-negativity constraint,  $(\lambda, \mathbf{f})$  is the scalar product of arrays and  $\gamma$  is the Lagrange multiplier associated with the flux constraint. It has been shown in [10] that the third term in the r.h.s. of Eq. (5) can be dropped because the constraint of flux conservation can be taken into account by a renormalization of the iterates (see below). Then, by writing the Kuhn–Tucker conditions (KTC) for the minimization of the reduced Lagrange function (without the  $\gamma$ -term), one gets necessary and sufficient conditions for the minimum points  $\mathbf{f}^*, \lambda^*$ :

$$\begin{aligned} \nabla_{\mathbf{f}} L(\mathbf{f}^*, \lambda^*; \mathbf{g}) &= 0 \iff \lambda^* = \nabla_{\mathbf{f}} J(\mathbf{f}^*; \mathbf{g}), \\ \mathbf{f}^*(m, n) &\geq 0, \quad \lambda^*(m, n) \geq 0, \\ \lambda^*(m, n) \mathbf{f}^*(m, n) &= 0, \end{aligned} \tag{6}$$

or, by eliminating the Lagrange parameters:

$$\mathbf{f}^* \nabla_{\mathbf{f}} J(\mathbf{f}^*; \mathbf{g}) = 0, \quad \mathbf{f}^*(m, n) \geq 0, \quad \nabla_{\mathbf{f}} J(\mathbf{f}^*; \mathbf{g})(m, n) \geq 0; \tag{7}$$

in the first relation the product of arrays is defined pixel by pixel.

We recall that, multiplication of  $[-\nabla_{\mathbf{f}} J(\mathbf{f}; \mathbf{g})]$  by a positive array provides again a descent direction of the functional. Therefore, the following array:

$$\mathbf{d}(\mathbf{f}; \mathbf{g}) = \frac{\mathbf{f}}{\mathbf{V}(\mathbf{f}; \mathbf{g})} [\mathbf{U}(\mathbf{f}; \mathbf{g}) - \mathbf{V}(\mathbf{f}; \mathbf{g})], \tag{8}$$

is a descent direction. In this equation, the representation of the gradient given in Eq. (4) is used; moreover, quotients and products are also defined pixel by pixel. Then the general structure of the descent algorithm, described in Lanteri et al. [11], is given by

- choose an initial  $\mathbf{f}^{(0)}$ , satisfying the constraints of Eq. (3) (in general, a uniform image);
- given  $\mathbf{f}^{(k)}$  compute:

$$\tilde{\mathbf{f}}^{(k+1)} = \mathbf{f}^{(k)} + \alpha^{(k)} \mathbf{f}^{(k)} \frac{\mathbf{U}(\mathbf{f}^{(k)}; \mathbf{g}) - \mathbf{V}(\mathbf{f}^{(k)}; \mathbf{g})}{\mathbf{V}(\mathbf{f}^{(k)}; \mathbf{g})}, \tag{9}$$

$$\tilde{c}^{(k+1)} = \sum_{m,n} \tilde{\mathbf{f}}^{(k+1)}(m, n), \tag{10}$$

- set:

$$\mathbf{f}^{(k+1)} = \frac{c}{\tilde{c}^{(k+1)}} \tilde{\mathbf{f}}^{(k+1)}. \tag{11}$$

In Eq. (11), the constant  $c$  is that defined in Eq. (3) and therefore Eq. (11) is the renormalization of the iterates taking into account the flux constraint, as indicated above. Moreover,  $\alpha^{(k)} = \alpha^{(k)}(m, n) > 0$  is an array of relaxation parameters, which can be changed at each iteration and provides the step in the descent direction. It is easy to compute the maximum step size  $\alpha_{\text{MAX}}^{(k)}$  ensuring the non-negativity of all the components of the iterates; it does not depend on  $m, n$  and it turns out that it is greater than 1. Finally, the convergence of the algorithm can be obtained if, at the iteration  $k$ , the step size is computed using a line search method in the range  $[0, \alpha_{\text{MAX}}^{(k)}]$ .

The algorithm takes a very simple form if we choose a unit step (i.e.  $\alpha^{(k)} = 1$ ); in such a case Eq. (9) is replaced by the following:

$$\tilde{\mathbf{f}}^{(k+1)} = \mathbf{f}^{(k)} \frac{\mathbf{U}(\mathbf{f}^{(k)}; \mathbf{g})}{\mathbf{V}(\mathbf{f}^{(k)}; \mathbf{g})}. \tag{12}$$

The convergence of this algorithm is not guaranteed in general, even if it can be proved in some particular cases; nevertheless it has been verified experimentally in all the applications we have considered. The most interesting feature of the algorithm is that *non-negativity of the iterates is automatically satisfied*, as one can easily verify.

### 2.1. Regularized functionals

In regularization theory [1] and in Bayesian approaches [8] the functional  $J(\mathbf{f}; \mathbf{g})$  has the following structure:

$$J(\mathbf{f}; \mathbf{g}) = J_0(\mathbf{f}; \mathbf{g}) + \mu J_R(\mathbf{f}), \tag{13}$$

where  $J_0(\mathbf{f}; \mathbf{g})$  is a discrepancy functional measuring the misfit between the detected image and the expected image associated with the object  $\mathbf{f}$ , as given by Eq. (1) (examples of discrepancy functionals will be given in the next subsections);  $J_R(\mathbf{f})$  is a regularization functional and  $\mu$  is the regularization parameter. With obvious notations we can write

$$\mathbf{U}(\mathbf{f}; \mathbf{g}) = \mathbf{U}_0(\mathbf{f}; \mathbf{g}) + \mu \mathbf{U}_R(\mathbf{f}), \quad \mathbf{V}(\mathbf{f}; \mathbf{g}) = \mathbf{V}_0(\mathbf{f}; \mathbf{g}) + \mu \mathbf{V}_R(\mathbf{f}), \tag{14}$$

$\mathbf{U}_0, \mathbf{V}_0$  being the arrays coming from the decomposition of the gradient of  $J_0(\mathbf{f}; \mathbf{g})$  and  $\mathbf{U}_R, \mathbf{V}_R$  those coming from the decomposition of the gradient of  $J_R(\mathbf{f})$ . By inserting these equations into Eq. (12), we obtain the following algorithm where the dependence on the regularization parameter is explicitly shown:

$$\tilde{\mathbf{f}}^{(k+1)} = \mathbf{f}^{(k)} \frac{\mathbf{U}_0(\mathbf{f}^{(k)}; \mathbf{g}) + \mu \mathbf{U}_R(\mathbf{f}^{(k)})}{\mathbf{V}_0(\mathbf{f}^{(k)}; \mathbf{g}) + \mu \mathbf{V}_R(\mathbf{f}^{(k)})}. \tag{15}$$

As far as we know, the convergence of this algorithm is not proved for  $\mu > 0$  and suitable discrepancy and regularization functionals, but convergence results exist for  $\mu = 0$  in the case of the discrepancy functionals discussed in the next subsections. Obviously convergence holds true also for the relaxed form of the algorithm given in Eq. (9). If one uses an approximate search method, such as the Armijo rule, for the estimation of the relaxation parameter, then the increase in computational cost can be acceptable.

### 2.2. Poisson noise

In the case of Poisson (photon) noise the maximization of the likelihood functional introduced by Shepp and Vardi [12] is equivalent to the minimization of the Csiszár directed divergence [4], which can be identified with the functional  $J_0(\mathbf{f}; \mathbf{g})$ , so that we have

$$J_0(\mathbf{f}; \mathbf{g}) = \sum_{m,n} \left\{ \mathbf{g}(m, n) \ln \left\{ \frac{\mathbf{g}(m, n)}{(\mathbf{A}\mathbf{f})(m, n) + \mathbf{b}} \right\} + [(\mathbf{A}\mathbf{f})(m, n) + \mathbf{b} - \mathbf{g}(m, n)] \right\}. \tag{16}$$

In such a case a possible choice of the arrays  $\mathbf{U}_0, \mathbf{V}_0$  is the following:

$$\mathbf{U}_0(\mathbf{f}; \mathbf{g}) = A^T \frac{\mathbf{g}}{\mathbf{A}\mathbf{f} + \mathbf{b}}, \quad \mathbf{V}_0(\mathbf{f}; \mathbf{g}) = \mathbf{1}, \tag{17}$$

where  $\mathbf{1}$  is the array whose elements are all equal to 1 (we have assumed that the PSF is normalized in such a way that the sum of all its pixel values is 1, so that  $A^T \mathbf{1} = \mathbf{1}$ ). If we insert these expressions into Eq. (12), we get:

$$\tilde{\mathbf{f}}^{(k+1)} = \mathbf{f}^{(k)} A^T \frac{\mathbf{g}}{\mathbf{A}\mathbf{f}^{(k)} + \mathbf{b}}. \tag{18}$$

The resulting algorithm is a very simple generalization of RLM taking into account background and flux normalization (which is automatic if the background is zero but not if the background is not zero). The convergence of EM, hence of RLM, has been proved by several authors [12,9,14].

### 2.3. Gaussian noise

In the case of Gaussian additive white noise, the maximization of the likelihood functional is equivalent to the minimization of the least-squares functional (see, for instance, [1]) which is given by:

$$J_0(\mathbf{f}; \mathbf{g}) = \|\mathbf{A}\mathbf{f} + \mathbf{b} - \mathbf{g}\|_2^2, \tag{19}$$

where  $\|\cdot\|_2$  denotes the usual Euclidean norm. In such a case it is easy to show that a possible choice of the  $\mathbf{U}_0, \mathbf{V}_0$  arrays is the following (again, we use the property  $\mathbf{A}^T \mathbf{b} = \mathbf{b}$ , due to the normalization of the PSF):

$$\mathbf{U}_0(\mathbf{f}; \mathbf{g}) = \mathbf{A}^T \mathbf{g}, \quad \mathbf{V}_0(\mathbf{f}; \mathbf{g}) = \mathbf{A}^T \mathbf{A} \mathbf{f} + \mathbf{b}. \quad (20)$$

If we insert these expressions into Eq. (12) we get:

$$\tilde{\mathbf{f}}^{(k+1)} = \mathbf{f}^{(k)} \frac{\mathbf{A}^T \mathbf{g}}{\mathbf{A}^T \mathbf{A} \mathbf{f}^{(k)} + \mathbf{b}}. \quad (21)$$

The result is a very simple generalization of ISRA, which takes into account both background and flux normalization. Convergence of ISRA was proved by De Pierro [5].

### 3. Reconstruction of images with high dynamic range

The accurate reconstruction of objects such as that shown in Fig. 1 is a difficult problem. In this case the important feature is that there is a large gap between the intensity of bright and faint objects and that these different objects are located in different image domains. Therefore, it is reasonable to consider regularization functionals containing a thresholding parameter which controls the regularizing effect of the functional in such a way that one gets a different kind of regularization in regions with very different object intensity. Of course the threshold, which is related to the gap between the intensity values, cannot be derived directly from the image; such an approach requires a preliminary reconstruction of the object (based on one of the standard methods, such as RLM or ISRA), whose result can be used for threshold estimation.

Our second requirement is that, in the faint regions, i.e. regions where the intensity is small with respect to the thresholding parameter, the regularized functional is approximated by the standard Tikhonov's regularization functional:

$$J(\mathbf{f}; \mathbf{g}) = J_0(\mathbf{f}; \mathbf{g}) + \mu \|\mathbf{f}\|^2, \quad (22)$$

where  $\mu$  is Tikhonov's regularization parameter.

To this purpose we consider regularization functionals with the following structure:

$$J_R(\mathbf{f}; \mathbf{g}) = \sum_{m,n} \Phi(\mathbf{f}(m, n)), \quad (23)$$

where  $\Phi(t)$  is a function which must be selected in order to satisfy the previous requirements, i.e. it must contain a threshold  $\eta$  such that  $\Phi(t) \simeq t^2$  for  $t$  small with respect to  $\eta$ . The functions considered in this paper are the following:

$$(i) \quad \Phi(t) = 2\eta^2 \left( \sqrt{1 + \frac{t^2}{\eta^2}} - 1 \right), \quad (24)$$

$$(ii) \quad \Phi(t) = \eta^2 \ln \left( 1 + \frac{t^2}{\eta^2} \right), \quad (25)$$

$$(iii) \quad \Phi(t) = \frac{t^2}{1 + (t^2/\eta^2)}. \quad (26)$$

The first is convex while the two others are not. It is easy to check that all the functions behave as  $t^2$  for small  $t$  and therefore are convex in a neighborhood of  $t = 0$ , which is the unique global minimum. We point out that these functions have been proposed for edge-preserving regularization; hence, in the original papers  $t$  is replaced by the modulus of the gradient. In particular function (i) is proposed in [3], function (ii) in [7] and function (iii) in [6]. In our case, since the regions of large gradient coincide with the regions of large values and the regions of small gradients coincide with the regions of small values of the object, we can replace  $t$  with the value of the object, as we do in Eq. (23).

**Remark 1.** The three functions above belong to a one-parameter family of functions defined by

$$\Phi(t, \alpha) = \frac{\eta^2}{1 - \alpha} \left\{ \left( 1 + \frac{t^2}{\eta^2} \right)^{1-\alpha} - 1 \right\}. \tag{27}$$

Function (i) is obtained for  $\alpha = \frac{1}{2}$ , function (ii) is the limit for  $\alpha = 1$  and, finally, function (iii) corresponds to  $\alpha = 2$ . We also point out that the limit for  $\alpha = 0$  is just the quadratic function related to Tikhonov regularization and that the transition from a convex to a non-convex function occurs at  $\alpha = \frac{1}{2}$ . In this way we have a family of functions connecting in a continuous way Tikhonov regularization to the other regularizations investigated in this paper.

It is clear that  $\eta$  is a thresholding parameter and that the functions provide a smooth reconstruction of the faint regions. On the other hand, when  $t$  is large with respect to  $\eta$ , we get

$$(i) \quad \Phi(t) \simeq 2\eta t, \tag{28}$$

$$(ii) \quad \Phi(t) \simeq 2\eta^2 \ln t, \tag{29}$$

$$(iii) \quad \Phi(t) \simeq \eta^2. \tag{30}$$

Therefore, we have regularization in terms of the 1-norm in the first case, a sort of logarithmic regularization in the second case and no regularization at all in the third case. In other words the three regularization functionals have a different behavior in the regions of high intensity.

If we compute now the gradient, we find that, in the cone of the non-negative  $\mathbf{f}$ , the arrays  $\mathbf{U}_R, \mathbf{V}_R$  have the following structure:

$$\mathbf{U}_R(\mathbf{f}) = \mathbf{0}, \quad \mathbf{V}_R(\mathbf{f}) = C \frac{\mathbf{f}}{(\eta^2 \mathbf{1} + \mathbf{f}^2)^\alpha}, \tag{31}$$

where the parameters  $C$  and  $\alpha$  are given in the three cases by the following expressions:

$$(i) \quad C = 2\eta, \quad \alpha = \frac{1}{2}, \tag{32}$$

$$(ii) \quad C = 2\eta^2, \quad \alpha = 1, \tag{33}$$

$$(iii) \quad C = 2\eta^4, \quad \alpha = 2. \tag{34}$$

By combining all possible expressions of the arrays  $\mathbf{U}, \mathbf{V}$  and inserting these expressions into Eq. (15) we obtain the regularized versions of RLM and ISRA corresponding to the regularization functionals introduced above. Since the array  $\mathbf{U}_R$  is zero, these algorithms take a very simple form and we write them here for the convenience of the reader:

- Regularized RLM

$$\tilde{\mathbf{f}}^{(k+1)} = \frac{\mathbf{f}^{(k)}}{\mathbf{1} + \mu \mathbf{V}_R(\mathbf{f}^{(k)})} \mathbf{A}^T \frac{\mathbf{g}}{\mathbf{A} \mathbf{f}^{(k)} + \mathbf{b}}. \tag{35}$$

- Regularized ISRA

$$\tilde{\mathbf{f}}^{(k+1)} = \mathbf{f}^{(k)} \frac{\mathbf{A}^T \mathbf{g}}{\mathbf{A}^T \mathbf{A} \mathbf{f}^{(k)} + \mathbf{b} + \mu \mathbf{V}_R(\mathbf{f}^{(k)})}. \tag{36}$$

The convergence of these algorithms has been verified experimentally in our numerical simulations.

#### 4. Numerical results

We have tested the algorithms above on the object of Fig. 1. The image has been generated by assuming the following situation. The object is observed in K-band by means of a 8.4 m perfect mirror, without effects of atmospheric turbulence.

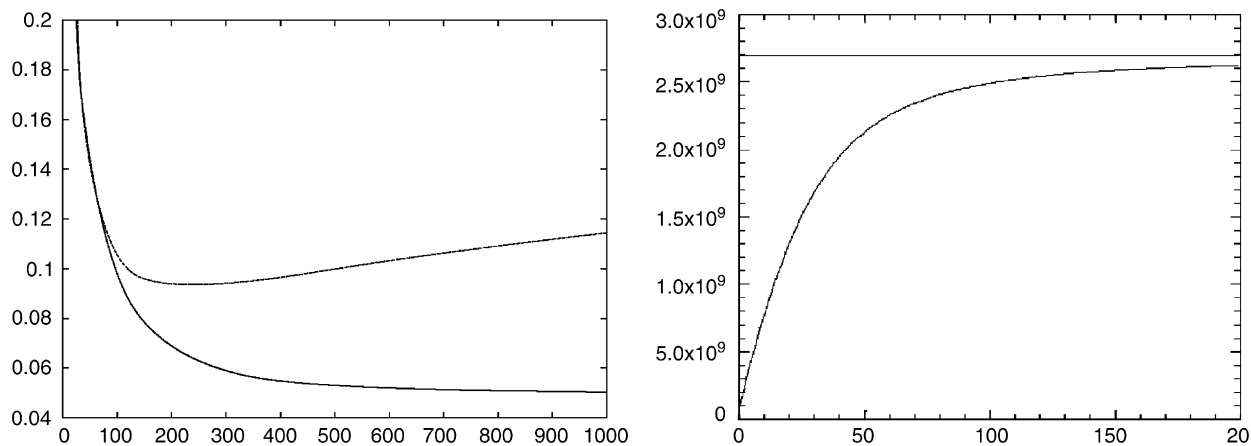


Fig. 2. Left panel: the relative r.m.s. error in the reconstruction of the ring as a function of the number of iterations both in the case of RLM (upper line) and in the case of non-convex regularization (lower line), with  $\eta = 5 \times 10^4$  and  $\mu = 1.2 \times 10^{-6}$ . Right panel: behavior of the flux of the primary star as a function of the number of iterations; the behavior is the same for RLM and the regularized algorithms.

Since the resolution of the telescope is 50 mas, we have assumed a slightly oversampled image with a pixel size of about 15 mas. The object is  $256 \times 256$ , whence with an angular extension of about  $3''$ . The angular separation of the binary is a bit greater than the angular resolution of the mirror and the magnitudes of the two stars are 10 and 11, respectively, while the integrated magnitude of the ring is about 15. To give an idea of the intensities involved in this object, we remark that the average number of photons per pixel in the ring is about 4000 while the number of photons emitted by the primary is of the order of  $10^9$ . Finally the image has been obtained by convolving the object with the Airy function of the mirror, by adding a background of 10 photons per pixel and by perturbing the result with photon (Poisson) and read-out (white Gaussian) noise. Here we assume a simplified version of the noise model described in [13].

The accuracy of the restoration has been checked by computing, at each iteration, the relative r.m.s. error in the reconstruction of the ring (2-norm of the difference between the original ring and the ring provided by the iteration, divided by the 2-norm of the original ring) as well as the flux of the primary star. The latter has been computed by integrating the reconstructed object over a  $3 \times 3$  square centered on the position of the primary.

We have first reconstructed the object by means of RLM. We reach a minimum value in the reconstruction error of the ring with about 240 iterations. The minimum value is of the order of 9.4%. Therefore this preliminary reconstruction, even if not very accurate, allows the estimation of the range of the possible values of  $\eta$ .

Next we used the regularized algorithm of Eq. (35) for each regularization functional of the previous section. We point out that the computational cost of one iteration of the regularized algorithm is approximately that of one iteration of RLM. For the choice of the thresholding parameter  $\eta$  and of the regularization parameter  $\mu$ , we looked for values minimizing the r.m.s. error in the reconstruction of the ring.

Since the maximum value of the ring is  $7 \times 10^3$ , we expect that the good values of  $\eta$  are greater than this value. This is true for the functionals (ii) and (iii) but not for the convex functional (i). In such a case we have found that it is possible to minimize the restoration error by means of a suitable choice of  $\mu$  if  $\eta = 6 \times 10^3$ . In the two other cases the restoration error does not strongly depend on  $\eta$  if  $\eta > 10^4$ . To fix a value, we have selected  $\eta = 5 \times 10^4$ .

For the value of  $\mu$ , we have found: in case (i), a minimum restoration error of 7.2% for  $\mu = 10^{-6}$ ; in cases (ii) and (iii), a minimum restoration error of about 5% for  $\mu = 1.2 \times 10^{-6}$ . Therefore, the regularization functionals (ii) and (iii) are essentially equivalent. Moreover, they provide a better reconstruction than the functional (i). Finally, all the functionals provide a good reconstruction of the binary, with an error in magnitude of about 3%.

In Fig. 2 (left panel) we plot the relative r.m.s. error in the reconstruction of the ring as a function of the number of iterations both in the case of RLM and in the case of the regularized algorithm provided by the functional (ii), with the best values of the parameters  $\eta$ ,  $\mu$ . It is evident that, while in the case of RLM there is a minimum (semiconvergence of the algorithm), hence an optimal value of the number of iterations, in the regularized case the algorithm is convergent. In Fig. 2 (right panel) we also plot the behavior of the flux of the primary star as a function of the number of iterations.

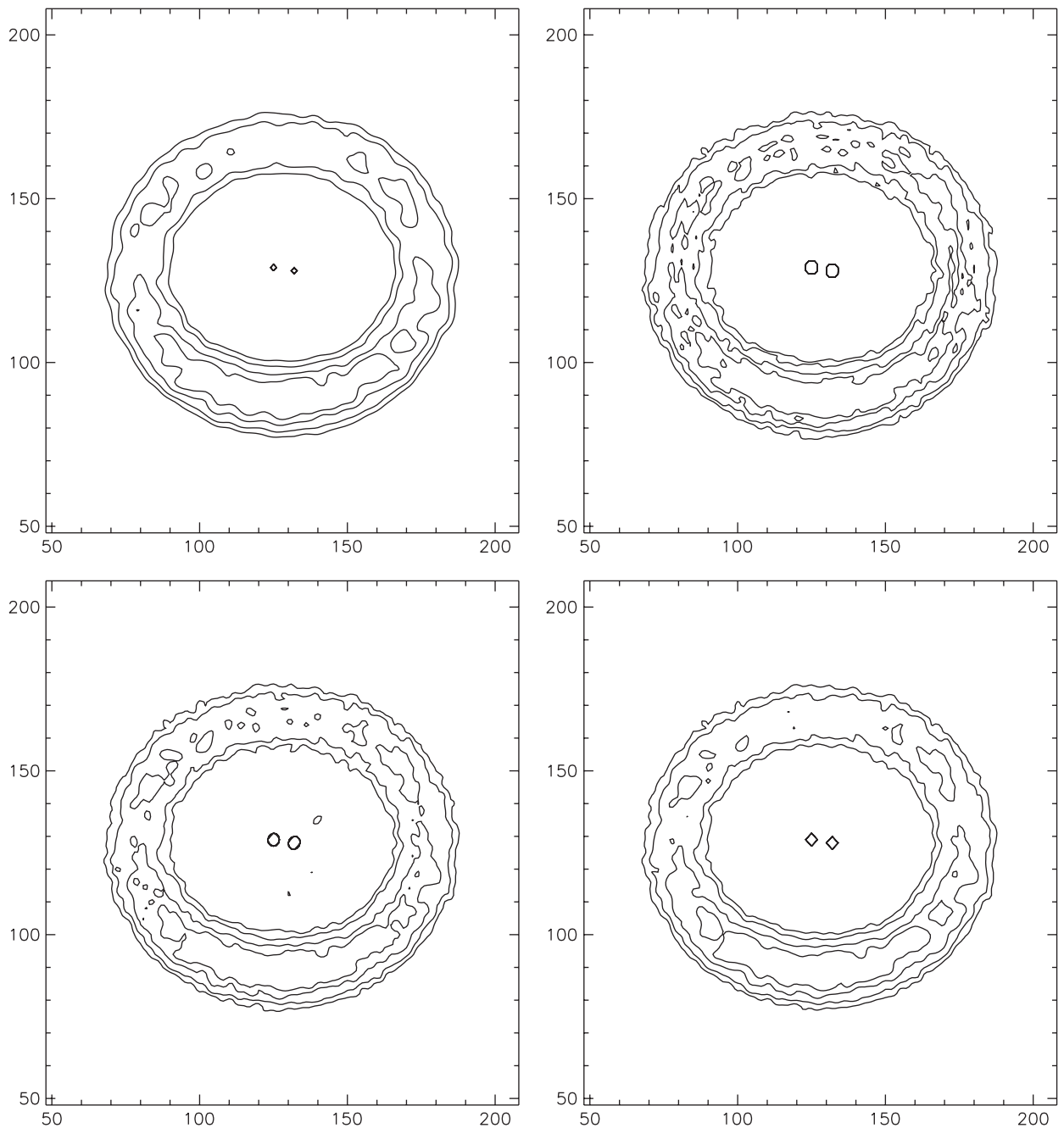


Fig. 3. Representation of the ring by means of level curves. The values corresponding to the plotted curves are given in the text. Upper-left panel: the object; upper-right: the reconstruction provided by RLM; lower-left: reconstruction with convex regularization; lower-right: reconstruction with non-convex regularization.

We plot only one curve because, for the reconstruction of this parameter, there is no visible difference between RLM and the three regularized algorithms. All algorithms converge to the correct value. In particular, the reconstruction of the magnitude is very fast, since this quantity is proportional to the logarithm of the flux. We obtain an error of 3% after 10 iterations and an error of 0.5% after 100 iterations.

In conclusion, if the parameters  $\eta$ ,  $\mu$  are accurately tuned, accurate reconstructions of the ring and of the binary are obtained with about 300 iterations. To give a more precise idea of the accuracy of the reconstructions of the ring provided

by the different methods, in Fig. 3 we represent the ring in term of level curves. We use four levels corresponding to the following values: 1430, 2160, 3510 and 4860. It is evident that the RLM reconstruction is affected by noise propagation and this effect is partly present also in the reconstruction provided by convex regularization. On the other hand the level curves obtained with non-convex regularization reproduce fairly well those of the original object.

Finally we have investigated ISRA and its regularized versions. Also in this case the computational cost of one iteration of the regularized algorithms approximately coincides with that of one ISRA iteration. Moreover, we remember that one ISRA iteration requires only 2 FFTs against the 4 required by one RLM iteration.

ISRA is not a natural method for the image we are considering since it is derived from an approach based on the assumption of white Gaussian noise. Therefore, it is not surprising to find that the best reconstruction of the ring provided by ISRA is much less accurate than that provided by RLM: the minimum reconstruction error is about 24% after 345 iterations. Moreover, the reconstruction is strongly affected by ringing effects.

On the other hand the three regularized approaches work well and have approximately the same behavior. The choice of  $\eta$  is not critical because, in all cases, values of  $\eta$  greater than the maximum value of the ring are acceptable. Therefore, in all cases, we have taken  $\eta = 5 \times 10^4$ . Moreover, in all cases, we obtain a minimum r.m.s of about 5% in the restoration of the ring with  $\mu = 1.6 \times 10^{-2}$ . This accuracy is just that provided by the regularized versions of RLM. The main difference is that the convergence is much slower. An error less than 6% is reached after 10,000 iterations and the 5% error is reached after 50,000 iterations. The magnitude of the primary is accurately reconstructed but also in this case one needs several thousands of iterations. Therefore these algorithms are time consuming and are not convenient from the computational point of view.

## 5. Concluding remarks

In this paper we have investigated different kinds of regularization of RLM and ISRA for the reconstruction of astronomical objects with high dynamic range. The tests have been performed using a particular model of young binary, shown in Fig. 1. In the case of RLM we have obtained the best results by means of a non-convex regularization. In the case of ISRA, results with a similar accuracy have been obtained by means of the same functionals but also by means of a convex regularization. However, the computational efficiency of the regularized version of RLM is superior to that of the regularized versions of ISRA. We point out that the computational cost of one iteration of the regularized RLM is approximately equal to that of one iteration of RLM and that the number of iterations required for obtaining the best reconstruction in the two cases is approximately the same. Therefore, the method proposed in this paper allows to improve significantly the results of RLM without increasing the computational cost.

In conclusion, RLM, combined with one of the non-convex regularizations proposed in this paper, seems to be a valuable approach to the reconstruction of astronomical objects with high dynamic range. Indeed, in such a case, the choice of the thresholding parameter is not critical and the computational cost is acceptable for astronomical applications.

## References

- [1] M. Bertero, P. Boccacci, *An Introduction to Inverse Problems in Imaging*, IOP Publishing, Bristol, 1998.
- [2] M. Carillet, S. Correia, P. Boccacci, M. Bertero, Restoration of interferometric images-II. The case-study of the large binocular telescope, *Astronom. and Astrophys.* 387 (2002) 744–757.
- [3] P. Charbonnier, L. Blanc-Feraud, G. Aubert, M. Barlaud, Deterministic edge-preserving regularization in computed imaging, *IEEE Trans. Image Processing IP-6* (1997) 298–311.
- [4] I. Csiszár, Why least squares and maximum entropy? An axiomatic approach to inference for linear inverse problems, *Ann. Statist.* 19 (1991) 2032–2066.
- [5] A.R. De Pierro, On the convergence of the iterative image space reconstruction algorithm for volume ECT, *IEEE Trans. Med. Im. MI-6* (1987) 174–175.
- [6] S. Geman, D. Mc Clure, Statistical methods for tomographic image reconstruction, in: *Proceedings of the 46th session of the ICI, Bulletin of the ICI*, 1987, pp. 5–21.
- [7] T. Hebert, R. Leahy, A generalized EM algorithm for 3-D Bayesian reconstruction from Poisson data using Gibbs prior, *IEEE Trans. Med. Im. MI-8* (1989) 194–202.
- [8] J.P. Kaipio, E. Somersalo, *Computational and Statistical Methods for Inverse Problems*, Springer, Berlin, 2004.
- [9] K. Lange, R. Carson, EM reconstruction algorithm for emission and transmission tomography, *J. Comp. Assisted Tomography* 8 (1984) 306–316.

- [10] H. Lanteri, M. Roche, C. Aime, Penalized maximum likelihood image restoration with positivity constraints: multiplicative algorithms, *Inverse Problems* 18 (2002) 1397–1419.
- [11] H. Lanteri, M. Roche, O. Cuevas, C. Aime, A general method to devise maximum-likelihood signal restoration multiplicative algorithms with non-negativity constraints, *Signal Process.* 81 (2001) 945–974.
- [12] L.A. Shepp, Y. Vardi, Maximum likelihood reconstruction for emission tomography, *IEEE Trans. Med. Im. MI-1* (1982) 113–122.
- [13] D.L. Snyder, A.M. Hammoud, R.L. White, Image recovery from data acquired with a charge-coupled-device camera, *J. Opt. Soc. Amer. A* 10 (1993) 1014–1023.
- [14] Y. Vardi, L.A. Shepp, L. Kaufman, A statistical model for Positron Emission Tomography, *J. Amer. Statist. Assoc.* 80 (1985) 8–20.